The diameters and velocities of the droplets ejected after splashing

Guillaume Riboux & José Manuel Gordillo†

Área de Mecánica de Fluidos, Departamento de Ingenería Aeroespacial y Mecánica de Fluidos, Universidad de Sevilla, Avenida de los Descubrimientos s/n 41092, Sevilla, Spain.

(Received ?? and in revised form ??)

When a drop impacts a smooth, dry surface at a velocity above the so-called critical speed for drop splashing, the initial liquid volume losses its integrity, fragmenting into tiny droplets violently ejected radially outwards. Here, we make use of the model in Riboux & Gordillo (2014), of a one-dimensional approximation for the flow in the ejected liquid sheet and of balances of mass and momentum at the border of the sheet, to calculate mean sizes and velocities of the ejected drops. The predictions of the model are in good agreement with experiments.

1. Introduction

By the end of the nineteenth century and making use of high speed photography Worthington (1908) pioneered the phenomenological description of very fast hydrodynamic events, like those caused by the impact of a drop against a solid, that take place, quoting Worthington, 'in the twinkle of an eye'. Recently, helped by the advances in high speed video imaging, a wealth of scientific papers have revealed unforeseen aspects of drop impact, among which one could cite the critical roles played by the structure of the solid surface Richard *et al.* (2002); Duez *et al.* (2007); Bird *et al.* (2013) or by the gaseous atmosphere in promoting or inhibiting the splash Xu *et al.* (2005); Mandre *et al.* (2009); Duchemin & Josserand (2011); Latka *et al.* (2012). During the past decades, many contributions have been devoted to deduce a criterion to decipher the precise conditions under which a drop hitting a solid surface either conserves its integrity after impact or disintegrates into smaller fragments Mundo *et al.* (1995); Rioboo *et al.* (2002); Josserand & Zaleski (2003); Xu *et al.* (2005); Yarin (2006); Bird *et al.* (2009); Mandre *et al.* (2009); Duchemin & Josserand (2011); Latka *et al.* (2012); Kolinski *et al.* (2012); Palacios *et al.* (2013); Driscoll *et al.* (2010). However, to our knowledge, the only splash criterion compatible with all the available experimental evidences and which predicts the splash threshold velocity with small relative errors for smooth dry surfaces, has only been deduced recently by Riboux & Gordillo (2014). The theory proposed, which is supported by a thorough experimental study as well as by the data published by Mundo *et al.* (1995); Xu *et al.* (2005); Palacios *et al.* (2013); Stevens (2014), shows that the critical impact velocity above which splashing occurs, takes place when the extremely thin and fast liquid sheet, which is expelled in the direction tangent to the solid as a consequence of the impact, is accelerated vertically up to velocities larger than those caused by the capillary retraction of the liquid rim. The vertical accelerations imparted to the edge of the spreading sheet, which possesses a characteristic thickness of the order of a hundredth of the drop radius, are produced by the lift force exerted by the surrounding gaseous atmosphere. The lift results from the addition of the lubrication force exerted between the

† Email address for correspondence: griboux@us.es & jgordill@us.es

	ρ (kg/m^3)	σ (mN/m)	μ (cP)	R (mm)	ℓ_σ (mm)	V^* (m/s)	$Oh \times 10^3$ (-)
(a)	789	22.6	1.0	1.04	1.71	2.19	7.3
(b)	854	17.2	1.3	0.86	1.43	1.70	11.4
(c)	913	18.6	4.6	0.89	1.44	1.69	37.1
(d)	1000	19.5	10.0	0.90	1.41	2.01	75.3

TABLE 1. Physical properties of the different fluids used, drop radius, capillary length, impact velocity for splashing and the corresponding Ohnesorge number, defined here as $Oh{=}\sqrt{We}/Re{=}\mu/\sqrt{\rho R\sigma}$. ($a$) Ethanol, ($b$) Decamethyltetrasiloxane, (c) Poly(Dimethylsiloxane) and (d) 10 cP Silicone Oil.

lamella and the substrate, which strongly depends on the mean free path between gas molecules, and on the aerodynamic forces acting at the top part of it Riboux & Gordillo (2014).

In this contribution we extend the theoretical results in Riboux & Gordillo (2014), from now on R&G, to provide a detailed analysis of the drop disintegration into tiny droplets taking place when the impact velocity is above the critical one. More precisely, the motivation of the present study is to express the velocities as well as the radii of the droplets ejected after the violent impact against the solid, as a function of the liquid and gas physical properties, the initial drop radius and the impact velocity.

The paper is structured as follows: in section §2 we present the phenomenological observations associated with the atomization of the splashing drop right after the impact, §3 is dedicated to develop a theoretical model which is validated by comparison with the experimental evidence in section §4, and §5 is devoted to present the conclusions.

2. Experimental study

Experiments are performed using the same setup as that employed in R&G, where spherical millimetric drops of radii R fall under the action of gravity onto a dry glass slide which is partially wetted by the liquids of physical properties provided in table 1, being the contact angle in all cases considered close to $\sim 20^o$ and $\nu = \mu/\rho$ will indicate from now on the liquid kinematic viscosity. The velocity V of the drops at the instant of impact is controlled by imposing the vertical distance between the exit of the needles and the substrate. The impact process is recorded using two high speed cameras, placed perpendicular to each other, and operated using two different optical magnifications and acquisition speeds (see R&G and the Appendix for details). Water is not included as one of the working fluids in our experimental study because the limitations in the spatial and temporal resolutions of our high speed cameras, impede an accurate measurement of the tiny sizes - just a few microns- and large velocities - ~ 20 m.s^{-1} - of the fragments ejected. Nonetheless, we will make use in Appendix B of the experimental results of splashing water droplets provided in Thoroddsen *et al.* (2012) to give further support to our theory.

Figure 1 shows the time sequence of events occurring right after a drop of a liquid with viscosity μ=1 cP falls onto the solid for increasing impact velocities. For the smaller value of V (figure 1, first column), a liquid sheet of thickness $H_t \ll R$, is expelled radially outwards and tangent to the wall with a velocity $V_t \gg V$ for $T \geqslant T_e$, with T_e the ejection time in R&G and $T = 0$ fixed at the instant when the drop first touches the substrate

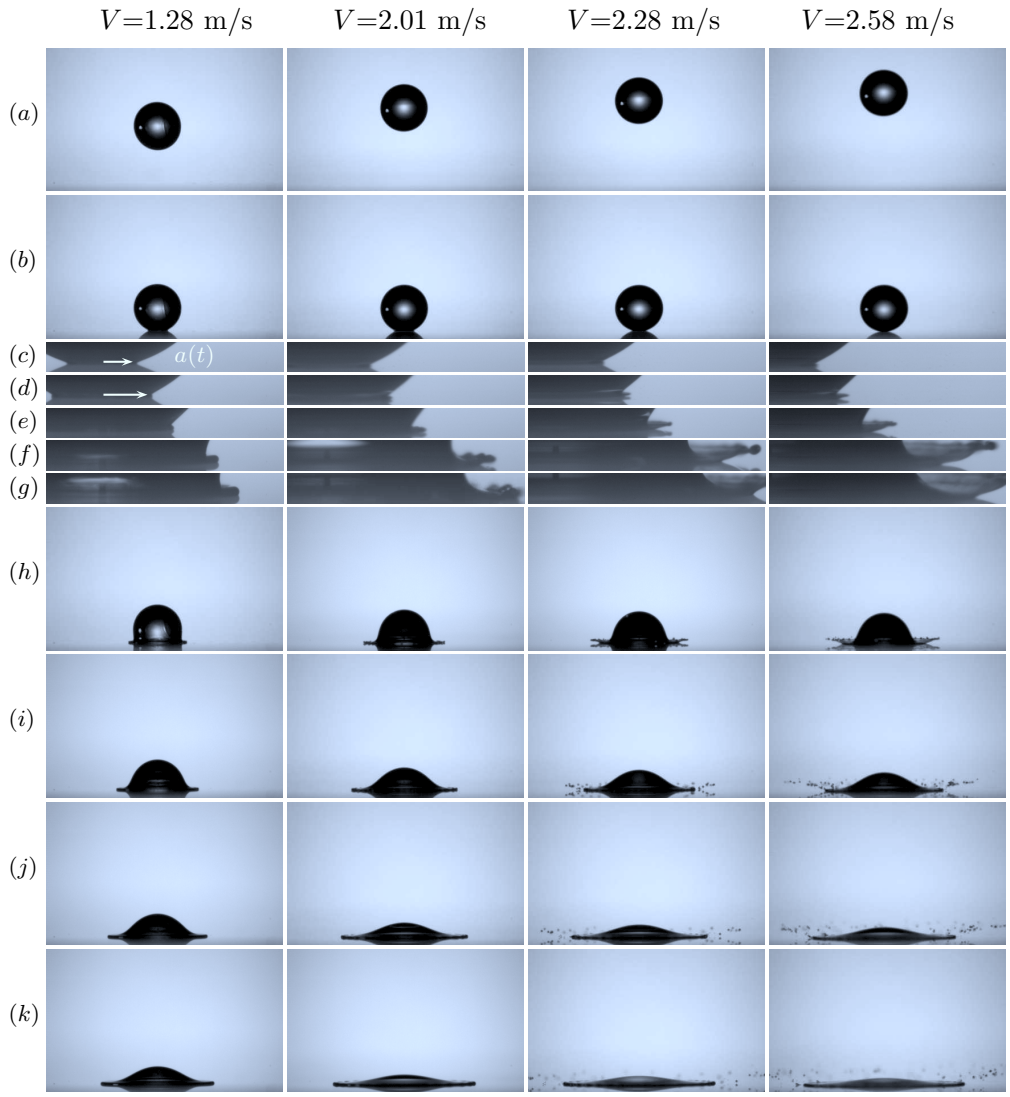

FIGURE 1. Effect of V on the splashing of the drop. Each image sequence corresponds to the instants (*a*) T=-1.131 ms, (*b*) 0.029 ms, (*c*) 0.03 ms, (*d*) 0.05 ms, (*e*) 0.09 ms, (*f*) 0.21 ms, (*g*) 0.28 ms, (*h*) 0.319 ms, (*i*) 0.609 ms, (*j*) 0.899 ms and (*k*) 1.189 ms. Images *c*–*g* possess a higher spatiotemporal resolution than the rest of the images in the same column. The temporal resolutions of each of the high speed cameras are 10 μs and 58 μs respectively. The liquid is ethanol and the radius of the drop is R=1.04 mm. The critical velocity for splashing is V^*=2.19 m/s.

(see figure 1). When the impact speed is slightly increased (figure 1, second column), the lamella first dewets the substrate (figure 1*f*, second column) to contact it again (figure 1*g*, second column) as a consequence of the radial growth of the rim caused by capillary retraction. For velocities above the critical impact speed (image sequence *a*–*k*, third column), the edge of the liquid sheet dewets the substrate and breaks into droplets of characteristic radii R_d. These droplets are ejected outwards at a velocity substantially larger than that of the impact (Figures 1*i*–*k*, third and fourth columns).

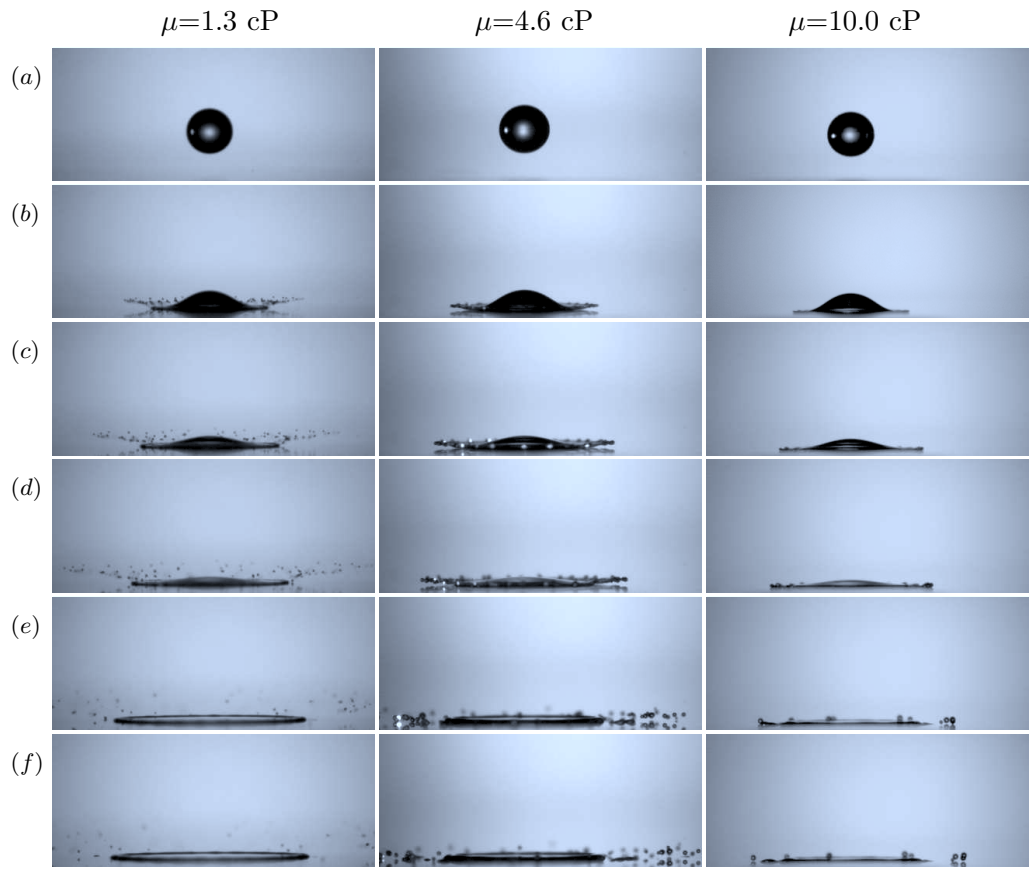

FIGURE 2. Effect of the viscosity μ on the splashing of a droplet for V=2.21±0.01 m/s and R=0.88±0.023 mm. Each image sequence correspond to the instants (*a*) T=-0.261 ms, (*b*) 0.609 ms, (*c*) 0.899 ms, (*d*) 1.189 ms, (*e*) 2.349 ms and (*f*) 2.929 ms. The temporal resolution is 58 μs.

Figure 2 shows the effect of varying the liquid viscosity by keeping the impact velocity and the drop radius at nearly constant values. The three cases illustrated correspond to impact velocities above the splash threshold namely, $V > V^*$. Figure 2 shows that an increase in liquid viscosity retards the instant at which droplets are first ejected and also decreases the small angle the droplets form with the substrate, suggesting that the vertical velocity component of the droplets is far smaller than the radial one. Figures 1–2 also reveal that the fragmentation process starts through the ejection of small droplets departing right from the rim bordering the radially expanding lamella. Thus, the disintegration of the edge of the liquid sheet, takes place in a fashion similar to that described by Villermaux & Bossa (2011) and Peters *et al.* (2013).

3. Modeling the drop ejection process

The first steps to describe the disintegration of the drop occurring during the initial instants after impact, are to determine the values of: i) the ejection time T_e, ii) the initial tangential velocity of the edge of the lamella, $V_t(T_e)$ and iii) its initial thickness, $H_t(T_e)$. For that purpose, we make use of the previous results in R&G where, choosing R, V,

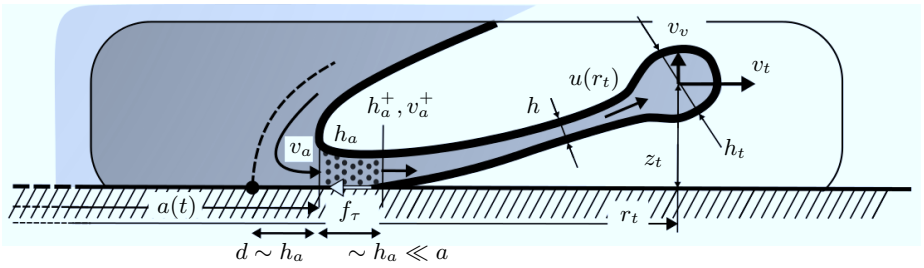

FIGURE 3. Sketch of the lamella for $T > T_e$ for $V > V^*$ i.e., for impact velocities above which the lamella dewets the substrate. This figure also illustrates the definitions of the different variables needed to describe the position of the rim as well as the region at the root of the lamella where the liquid is decelerated by viscosity. Note that since $a \propto t^{1/2}$ and $h_a \propto t^{3/2}$, $h_a \ll a$ for $t \ll 1$. The discontinuous line, located at a distance $d \propto t^{3/2} \propto h_a$ from the jet root, limits the region from which fluid particles feed the lamella.

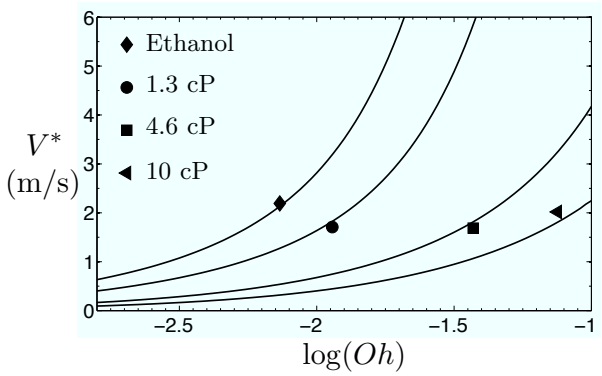

FIGURE 4. Experimental values of the critical impact velocities V^* for different values of the Ohnesorge number. The legend indicates the different fluids listed in table 1. Continuous lines indicate the results of the model presented in R&G.

R/V, ρV^2 as characteristic scales of length, velocity, time and pressure, with ρ the liquid density and lower-case letters denoting dimensionless variables, it is shown that:

i. The radius of the circular area indicated in figures 1 and 3 evolves in time as $a = \sqrt{3\,t}$. For $T < T_e$ namely, before the lamella is ejected, $a(t)$ indicates the radius of the wetted area (figure 1). For $T > T_e$, a is the distance between the drop axis of symmetry and the radial position where the root of the lamella is located; therefore, $a < r_t$, with r_t the radial position of the rim (see figure 3).

ii. The tangential velocity at which the lamella is initially ejected is $v_t(t_e) \simeq \dot{a}(t_e) = 1/2\sqrt{3/t_e}$.

iii. The thickness of the edge of the lamella at the instant of ejection is $h_t \simeq \sqrt{12} t_e^{3/2}/\pi$.

iv. Since $v_t = \dot{a}$ at $t = t_e$ namely, that the wetted area and the tip of the lamella advance at the same speed, and due to the fact that the lamella can only be ejected if its tip advances faster than the radius of the wetted area, t_e is calculated through

$$c_1\, Re^{-1}\, t_e^{-1/2} + Re^{-2}\, Oh^{-2} = \ddot{a}\, h_t^2 = c^2 t_e^{3/2}\,, \tag{3.1}$$

which expresses that the ejection time is the instant at which the deceleration of the edge of the lamella coincides with the deceleration of the wetted area, $\ddot{a}$. In equation

(3.1), $Re = \rho V R/\mu$ and $Oh = \mu/\sqrt{\rho R \sigma}$ denote, respectively, the impact Reynolds and Ohnesorge numbers, σ is the interfacial tension coefficient and $c_1 \simeq \sqrt{3}/2$ and $c^2 = 1.2$ are constants adjusted experimentally. In R&G it was also shown that the ejection time given by equation (3.1) possess the following high-Oh and low-Oh limits, respectively given by $t_e = 2\,Re^{-1/2}$ and $t_e \propto Re^{-4/3}Oh^{-4/3}$.

Moreover, in R&G it is shown that, once the sheet is ejected, its edge experiences a *vertical* lift force per unit length ℓ

$$\ell = K_l\,\mu_g\,V_t + K_u\,\rho_g\,V_t^2\,H_t \tag{3.2}$$

which results from the addition of the lubrication force exerted by the gas in the wedge region located between the advancing lamella and the substrate, $K_l\mu_g\,V_t$, and the suction force exerted by the gas at the top part of it, $K_u\,\rho_g\,V_t^2\,H_t$. Here, the subscript g represents gas quantities, $K_u \simeq 0.3$ is a constant determined numerically and the expression

$$K_l \simeq -(6/\tan^2(\alpha))\left[\ln\left(19.2\lambda/H_t\right) - \ln\left(1 + 19.2\lambda/H_t\right)\right], \tag{3.3}$$

with λ denoting the mean free path of gas molecules, is deduced using lubrication theory once it is assumed that the front part of the lamella can be approximated to a wedge of constant angle $\alpha \sim 60^\circ$ while it is in contact with the substrate. Let us point out here that α refers here to the angle the advancing front forms with the substrate at the instant of ejection t_e (see R&G for details) and, thus, α is not related with the angle at which drops are ejected. Indeed, the ejected droplets form an angle with the substrate which can be approximated by the ratio between their vertical and horizontal velocity components.

Thus, the force balance projected in the vertical direction, $\rho\,H_t^2\dot{V}_v \propto \ell$, with ℓ given by (3.2), provides the vertical velocity at which the lamella is *initially* expelled, namely,

$$V_v(T_e) = C_v\sqrt{\ell/\left(\rho\,H_t\right)}\,. \tag{3.4}$$

As it is shown by R&G, the good agreement with their own experimental data as well as with those in Mundo *et al.* (1995); Palacios *et al.* (2013); Xu *et al.* (2005); Stevens (2014), indicates that the critical impact velocity V^* above which the drop disintegrates into droplets, results from imposing that the vertical velocity (3.4) is such that $V_v/V_r \sim O(1)$, a condition resulting in $\sqrt{\ell/(2\sigma)} \simeq 0.14$, with $V_r = \sqrt{2\sigma/\rho\,H_t}$ the capillary retraction velocity (Taylor 1959; Culick 1960). Figure 4, which shows the comparison between the splash threshold velocity V^* predicted by $\sqrt{\ell/(2\sigma)} \simeq 0.14$ with ℓ given by equation (3.2) and that measured experimentally for each of the four fluids listed in table 1, give further support to our results in R&G. From now on, we will focus only on the description of the drop fragmentation process for values of the velocity ratio $V/V^* > 1$.

So far, the theory in R&G has been tested for impact velocities below or equal to the critical speed, so it is first necessary to check whether the theory is equally applicable to calculate the initial values of $V_v(T_e)$ and $V_t(T_e)$ for $V > V^*$. We will show below that there exists a very good agreement between experiments and the theoretical values and thus, the next step in our purpose to determine the velocities and sizes of the fragments ejected from the rim, is to describe the liquid flow within the lamella formed for $t > t_e$ and extending from $r = a(t)$ to $r = r_t > a$ (see figure 3).

In R&G it is also shown that, when viscous effects are neglected, the thickness of the lamella and the liquid velocity at $a = \sqrt{3\,t}$ i.e., at the radial position where the root of the lamella is located, are respectively given by

$$h_a = \frac{\sqrt{12}}{3\pi}\,t^{3/2} \quad \text{and} \quad v_a = \sqrt{3/t}\,, \tag{3.5}$$

being these equations valid for $a \lesssim 1$, namely, $t \lesssim 1/3$. However, in a real fluid, a boundary layer of dimensional thickness $\Delta \sim \sqrt{\nu\, T_r} = \sqrt{\nu R/V}(h_a/v_a)^{1/2}$, with $T_r \sim R/V h_a/v_a$ the characteristic residence time of fluid particles entering the lamella, develops in the region $r \simeq \sqrt{3t}$. Indeed, from equation (6) in the Supplementary Material in R&G, it can be deduced that, in the frame of reference moving at $V\dot{a}$, there exists a stagnation point in the flow at a dimensionless distance d from the root of the lamella such that $\sqrt{a}d^{-1/2} \sim \dot{a} \Rightarrow d \propto t^{3/2} \propto h_a \ll \sqrt{3t}$ (see figures 1 and 3). Note that Δ is the width of a boundary layer developing in a region of dimensionless width similar to the only relevant length scale characterizing this spatial region, i.e., the height of the root of the lamella. The effect of the viscous shear force per unit length exerted in this region, namely, $F_\tau = \rho V^2 R f_\tau \sim \mu\, V\, R/\Delta\, v_a\, h_a$, is to decrease the liquid velocity from v_a down to v_a^+ (see figure 3) and to increase the height of the lamella from h_a up to h_a^+ with the expressions of v_a and h_a given in (3.5). To relate the downstream quantities v_a^+ and h_a^+ with their corresponding upstream values, we make use of integral balances of mass and momentum applied at the shaded region of figure 3, yielding $h_a\, v_a = h_a^+\, v_a^+$ and $h_a\, v_a^2 - f_\tau = h_a^+\, (v_a^+)^2$. Therefore, equations

$$v_a^+ = v_a \left(1 - \sqrt{2}/\sqrt{Re\, v_a\, h_a}\right) , \quad h_a^+ = h_a \left(1 - \sqrt{2}/\sqrt{Re\, v_a\, h_a}\right)^{-1} , \tag{3.6}$$

constitute the initial conditions to be used next to predict the spatiotemporal evolution of the lamella, with $\sqrt{2}$ a fixed proportionality constant and v_a and h_a given in equation (3.5). In equation (3.6), the viscous deceleration term is of order $\sim O(0.1)$ for the liquid with the smallest viscosity and ~ 0.5 for the liquid with $\mu = 10$ cP.

To describe the dynamics of the portion of the liquid sheet extending from $r \simeq a(t)$ up to the radial position where the rim is located, namely, $r = r_t$, we make use of the fact that the viscous shear stresses can be neglected in this region because the liquid is no longer in contact with the substrate (see the sketch in figure 3 and the images *d* and *e* in figure 1, third and last columns). Additionally, since the local Weber number characterizing the flow within the sheet is such that $We\, (v_a^+)^2\, h_a \gg 1$, with $We = Re^2\, Oh^2$ the Weber number, the gradients of capillary pressure are negligible and, thus, the momentum equation within the lamella reduces to

$$\frac{\mathrm{D}u}{\mathrm{D}t} = 0 , \tag{3.7}$$

with $u(r,t)$ denoting the liquid velocity inside the lamella and $\mathrm{D}/\mathrm{D}t \equiv \partial/\partial\, t + u\partial/\partial r$ the material derivative. Equation (3.7) states that fluid particles conserve their velocities for $\sqrt{3t} \lesssim r < r_t(t)$ i.e., up to the radial position $r_t(t)$ where the rim is located. The equation for the thickness of the liquid sheet $h(r,t)$ in the region $\sqrt{3t} \lesssim r < r_t(t)$, is deduced making use of the mass balance, to yield

$$\frac{\partial\,(rh)}{\partial t} + \frac{\partial\,(rhu)}{\partial\, r} = 0 \Rightarrow \frac{\mathrm{D}\ln(rh)}{\mathrm{D}\,t} = -\frac{\partial\, u}{\partial\, r} . \tag{3.8}$$

Equations (3.7)–(3.8) representing the ballistic motion of fluid particles along the lamella, are solved subjected to the initial conditions $u(r = \sqrt{3t}, t) = v_a^+$ and $h(r = \sqrt{3t}, t) = h_a^+$, with v_a^+ and h_a^+ given in equation (3.6). Notice that, since $h_a \ll \sqrt{3t}$, we impose the boundary condition at $r = a(t)$ and neglect the width of the region $\sim O(h_a)$ where the boundary layer develops. To find the solution of the system (3.7)–(3.8), we used a Lagrangian numerical method which is quite similar to that described in Gekle & Gordillo (2010).

The radial and vertical positions of the edge of the lamella, $r_t(t)$ and $z_t(t)$ respectively, as well as its thickness, $h_t(t)$, are deduced applying the integral balances of mass and

momentum at the rim (Taylor 1959),

$$\begin{aligned} &\frac{\pi}{4}\frac{\mathrm{d}h_t^2}{\mathrm{d}t} = \left[u(r_t) - v_t\right] h(r_t)\,, \quad \frac{\mathrm{d}r_t}{\mathrm{d}t} = v_t\,, \\ &\frac{\pi\, h_t^2}{4}\frac{\mathrm{d}v_t}{\mathrm{d}t} = \left[u(r_t) - v_t\right]^2\, h(r_t) - 2\,We^{-1}\,. \end{aligned} \tag{3.9}$$

In equations (3.9), the geometry of the rim has been approximated to that of a torus of minor radius $h_t(t)/2$. Moreover, the smallness of the angle the spray forms with the substrate, suggests to approximate the projection of the capillary force per unit length in the direction tangent to the wall by $\simeq 2\sigma$ and, as a consequence of the smallness of the ratio ρ_g/ρ, air drag is neglected with respect to the flux of momentum entering the lamella. Equations in (3.9) need to be complemented with the force balance in the vertical direction

$$\frac{\pi\, h_t^2}{4}\frac{\mathrm{d}v_v}{\mathrm{d}t} = -2\,We^{-1}\frac{z_t}{r_t} + \frac{1}{2}\frac{\rho_g}{\rho}\,C_l\,v_t^2\,h_t \quad \text{with} \quad \frac{\mathrm{d}z_t}{\mathrm{d}t} = v_v\,, \tag{3.10}$$

where the projection of the capillary force per unit length in the direction normal to the wall, has been approximated by $\simeq 2\sigma z_t/r_t$ and the lift coefficient has been taken as a constant, $C_l = 1$. We assume that the influx of vertical momentum into the rim is negligible and, to simplify the model as much as possible, we do not take into account the dependence of C_l neither with the angle of incidence nor with the Reynolds number because our description does not retain the orientation of the tip of the lamella with respect to the surrounding atmosphere. Since, as it will be shown below, the theory in R&G is also valid to describe the ejection of the lamella for impact velocities above the critical one, equations (3.9)–(3.10) are solved subjected to the following initial conditions

$$\begin{aligned} &r_t = \sqrt{3\,t_e}\,, \quad z_t = 0\,, \quad h_t = \sqrt{12}\,t_e^{3/2}/\pi\,, \\ &v_t = 1/2\sqrt{3/t_e}\,, \quad v_v = 2\sqrt{\ell/\left(\rho\,H_t\,V^2\right)}\,, \end{aligned} \tag{3.11}$$

where t_e is calculated using equation (3.1) for μ <10 cP and $t_e = 2Re^{-1/2}$ for μ =10 cP.

The final step to complete our theory is to model the breakup time t_b, i.e, the time at which drops are ejected from the edge of the lamella. In Lhuissier & Villermaux (2011); Agbaglah *et al.* (2013); Peters *et al.* (2013) and references therein, it is clearly shown that the droplets composing the spray result from the amplification of Rayleigh–Taylor and capillary instabilities developing in the azimuthal direction Thoroddsen *et al.* (2012). The growth rates of these instabilities, however, are highly attenuated as a consequence of simultaneous growth of the rim thickness. Thus, drops will only be ejected when the time characterizing the radial growth of the rim, $T_h = \left(1/H_t\,\mathrm{d}H_t/\mathrm{d}T\right)^{-1}$, is substantially larger than either the capillary time $T_c = \left(\rho\,H_t^3/8\sigma\right)^{1/2}$ or the viscous time $T_v = \mu\,H_t/\sigma$. In the present case, since the local Ohnesorge number is such that $T_v/T_c = \mu/\sqrt{\rho\,H_t\,\sigma} \ll 1$, the growth of perturbations will be controlled by the capillary instead of by the viscous time. Figure 5 shows the time evolution of $T_c/T_h(t) = \sqrt{We/8}\,\left(h^{1/2}\right)\mathrm{d}h/\mathrm{d}t$, calculated through equations (3.7)–(3.10) and solved subjected to the initial conditions (3.6) and (3.11) for the different experimental conditions investigated. The function $T_c/T_h(t)$, reaches a constant value ~ 0.075 for times $T \approx T_b$, with T_b such that $\mathrm{d}/\mathrm{d}T[T_c/T_h](T = T_b) = 0$. In our model, we assume that drops will be ejected precisely at t_b. This choice for t_b is justified taking into account the following facts (Eggers & Villermaux (2008)): i) the characteristic time of growth of a capillary instability is $\sim 3\,T_c$, ii) Rayleigh's stability analysis of capillary perturbations reveal that the dimensionless wavenumber k with a fastest growth rate is $k = \pi H_t/\lambda \simeq 0.7$, with λ indicating

the wavelength of the perturbation, which is kept constant in time and iii) the growth of capillary instabilities is inhibited for $k \geqslant 1$. Therefore, in order for capillary corrugations with characteristic initial wavenumbers $k = 0.7$ to be amplified up to the point that drops are ejected from the rim, it is necessary that, in a time $3\,T_c$, the variation of the dimensionless wave number is such that $\Delta k < 0.3$. This condition is equivalent to $\mathrm{d}H_t/\mathrm{d}T \times 3T_c \lesssim 0.3H_t \Rightarrow T_c/T_h \lesssim 0.1$, a value which is very close and slightly larger than the minimum value of T_c/T_h, ~ 0.075. Note from figure 5 that our criterion to choose the instant of drop ejection, is consistent with the previous arguments. However, the way T_b is calculated is nothing but a plausible assumption: indeed, in a real experiment, the breakup time will strongly depend on the initial amplitude of azimuthal perturbations. Moreover, the determination of T_b from very flat curves as those in figure 5 may result in a non negligible uncertainty in the determination of the breakup time.

Moreover, since $T_c \ll T_b$, drops will be ejected slightly after T_b is reached. Thus, we neglect the contribution of T_c and assume that drops will be ejected right at T_b, with their velocities and sizes determined from the solution of equations (3.7)–(3.10) subjected to the initial conditions (3.6) and (3.11) particularized at the instant $t_b{=}T_b\,V/R$. Let us point out that, in our description, we assume that the mean diameters of the first drops ejected can be approximated to the thickness of the rim at $t = t_b$. The reason behind this approximation is the following: the volume of liquid contained in the rim of diameter $h(t_b)$ along a distance in the azimuthal direction equivalent to that of the most unstable capillary wavelength ($\simeq 4.5h(t_b)$) would give rise to the ejection of a droplet with a diameter $\simeq 1.9h_t(t_b)$. However, only a fraction of this volume will be ejected as a droplet; in fact, the simulations in Agbaglah *et al.* (2013) and the experiments in Thoroddsen *et al.* (2012) show that the diameter of the drops ejected is rather similar to that of the diameter of the rim, being this the reason why, in our model, we identify the diameter of the drops with that of the rim at $t = t_b$.

Figure 6, which shows the comparison of the measured ejection time with the value of t_b calculated as $\mathrm{d}/\mathrm{d}t\left[h^{1/2}\mathrm{d}h/\mathrm{d}t\right](t = t_b) = 0$, being t_b marked with a circle in figure 5 for each of the four fluids investigated and for different impact velocities, validates our approach.

4. Comparison between observations and the model

Figures 7–8 show the horizontal (v_t) and vertical (v_v) velocity components of the tip of the lamella at the instant of ejection, t_e, and also at the breakup time, t_b, for each of the four fluids investigated. The tangential and vertical velocities at t_e are respectively calculated through $v_t(t_e) = \dot{a}(t_e) = 1/2\sqrt{3\,t_e}$ and equation (3.4), with $C_v = 2$ and t_e determined either using equation (3.1) for μ <10 cP or by means of the high Oh limit $t_e = 2\,Re^{-1/2}$ for μ =10 cP. The results shown in figures 7–8 imply that the theoretical description of the ejection of the lamella in R&G, can be indeed extended to describe the drop fragmentation process for impact velocities above the critical one, namely, for $V > V^*$. Moreover observe that, for a given fluid, $v_t(t_e) \gg v_v(t_e)$, a fact indicating that the trajectory of the edge of the lamella forms a small angle with the substrate, in accordance with the experimental evidences of figures 1 and 2. This observation is more clearly depicted in figures 9–10, where the measured radial (r_t) and vertical (z_t) positions of the edge of the lamella are compared with our predictions. Note that the agreement is remarkable for each of the four fluids investigated and also that, as it was anticipated above, $z_t \ll r_t$. Moreover, the trajectories of the tip of the lamella in figures 9–10, represented up to $t = 0.4 > 1/3$, are calculated consistently with the range of

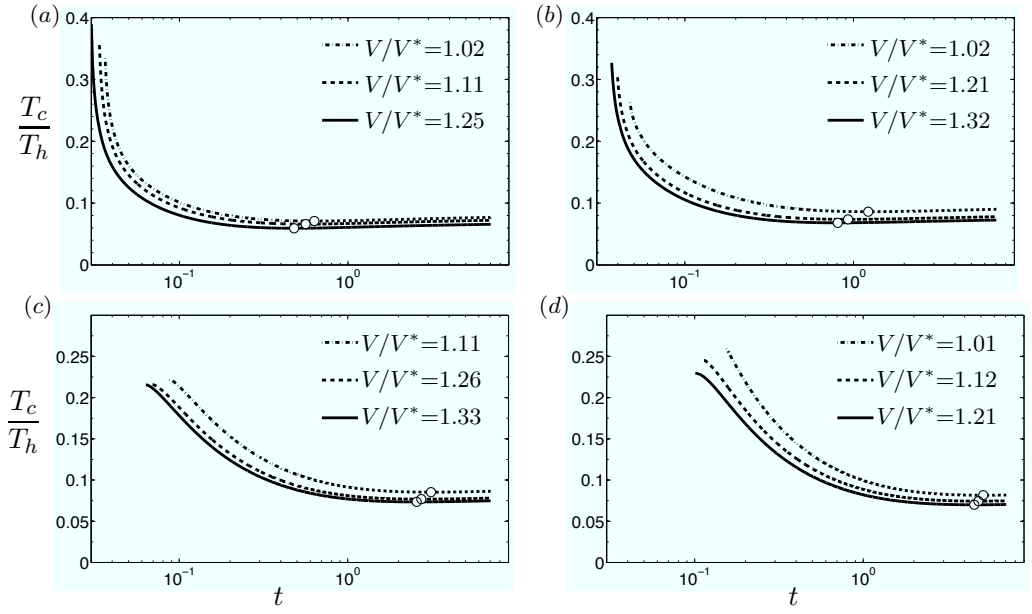

FIGURE 5. Calculated ratio $T_c/T_h = \sqrt{We/8}\left(h^{1/2}\right)\mathrm{d}h/\mathrm{d}t$ for different impact velocities and the different liquids considered in the experimental study: (a) Ethanol, (b) Decamethyltetrasiloxane, (c) Poly(Dimethylsiloxane) and (d) 10 cP Silicone Oil. The circles ($\circ$) indicate the instants t_b=$T_b\,V/R$ at which the model predicts when the droplets are ejected. Each of the curves in the figure start at t_e.

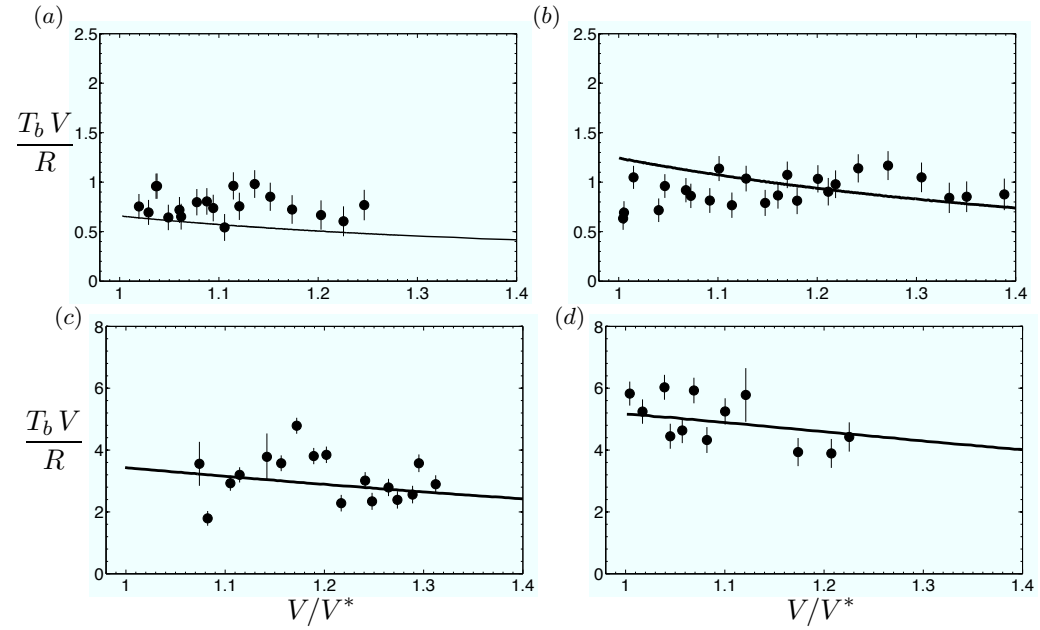

FIGURE 6. Comparison of the predicted breakup time t_b with the experimental one for (a) Ethanol, (b) Decamethyltetrasiloxane, (c) Poly(Dimethylsiloxane) and (d) 10 cP Silicone Oil.

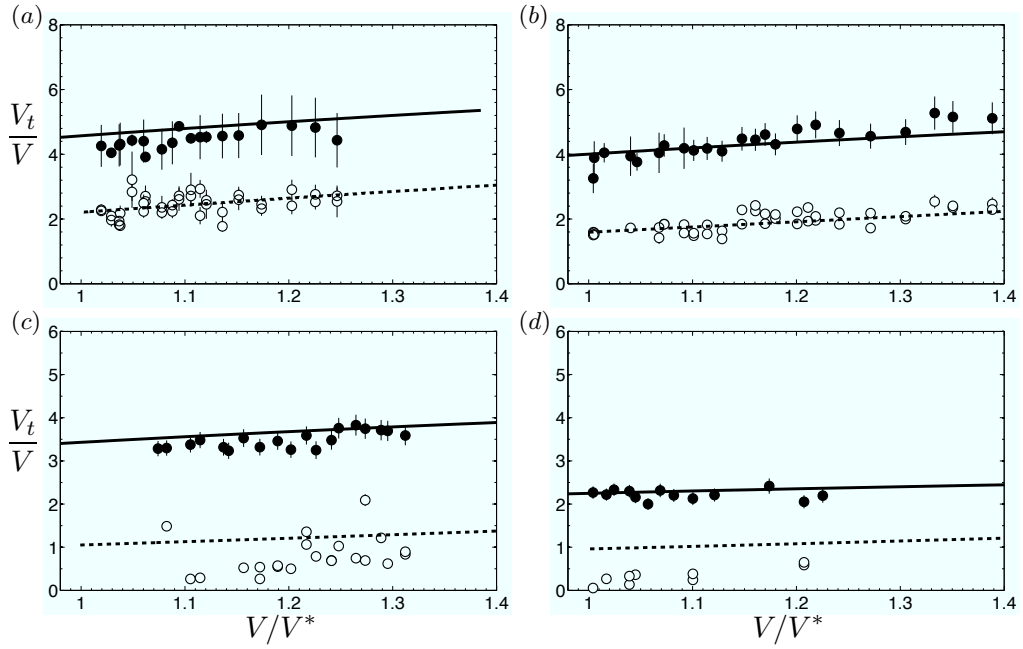

FIGURE 7. Tangential velocity of the lamella for impact velocities larger than the critical one, V^*, at the ejection time $t = t_e$ (•) and at the break-up instant $t = t_b$ (○). (*a*) Ethanol, (*b*) Decamethyltetrasiloxane, (*c*) Poly(Dimethylsiloxane) and (*d*) 10 cP Silicone Oil, with lines indicating the results of the model.

validity of equations (3.5). Indeed, figure 11 shows that the fluid particles entering the rim at the instant t, were ejected from the root of the jet at $t_a < 1/3$.

Figures 7–8 also reveal that, while $v_t(t_e)$ increases slightly with V/V^*, $v_v(t_e)$ remains practically unchanged within the range of impact velocities investigated. Also, note from figures 7–8 that both $v_t(t_e)$ and $v_v(t_e)$ decrease when increasing the liquid viscosity. Observe that all the experimental measurements at t_e are captured by our theory not only qualitatively, but also quantitatively.

But, the main purpose of our model is to predict the horizontal and vertical velocity components as well as the diameters of the droplets formed at the edge of the lamella. Figures 7–8 show that, as a consequence of the capillary deceleration of the rim, $v_t(t_e) > v_t(t_b)$ and that $v_v(t_e) > v_v(t_b)$ with the velocities at t_b calculated solving the system of equations (3.7)–(3.10) subjected to the initial values predicted by our theory i.e., equations (3.6) and (3.11). The agreement of our theory with the experimental measurements is quantitative for the all the fluids listed in table 1 except for the liquid with the largest viscosity.

The reason for the discrepancies with the liquid of $\mu = 10$ cP is probably related to the fact that the breakup time in this case is so large that $t_a > 1/3$, thus exceeding the limit of validity of equations 3.5 (see figure 11). Therefore, for $t_a > 1/3$, the equations in (3.5) should be substituted, for instance, by analogous expressions like those in Eggers *et al.* (2010). This step is beyond the scope of this study which, as it has been shown above, very well captures the sizes and velocities of the drops ejected in the cases of low viscosity liquids.

In spite of the fact that the model is unable to accurately predict the velocities of the fragments ejected for μ=10 cP, it is noteworthy that our approach predicts quantitatively

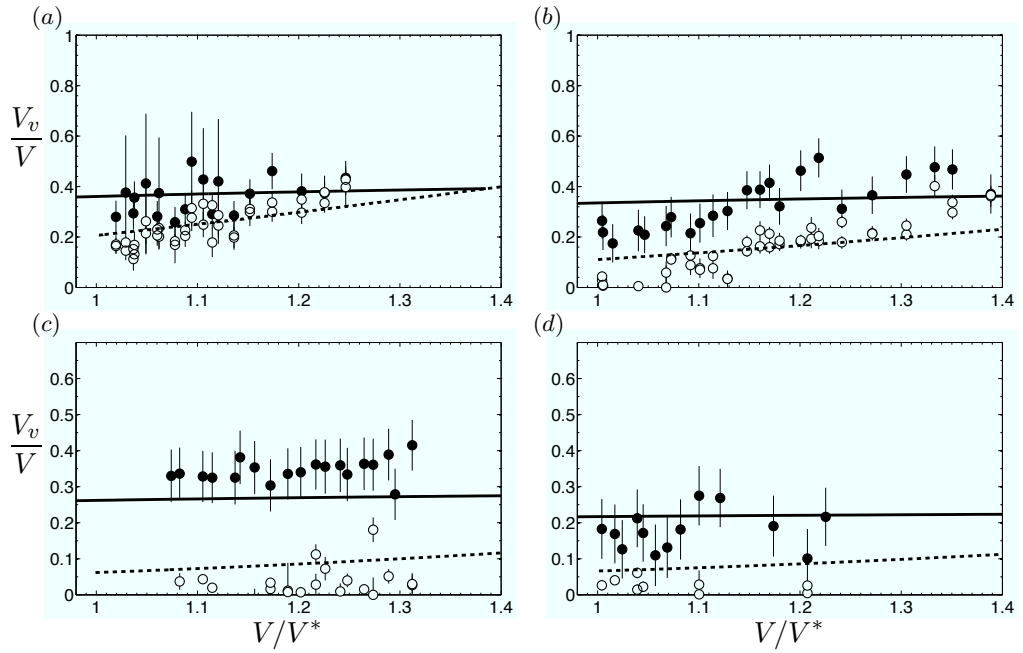

FIGURE 8. Vertical velocity of the lamella for impact velocities larger than the critical one, V^* at the ejection time $t = t_e$ (•) and at the break-up instant $t = t_b$ (○). (*a*) Ethanol, (*b*) Decamethyltetrasiloxane, (*c*) Poly(Dimethylsiloxane) and (*d*) 10 cP Silicone Oil with lines indicating the results of the model.

the sizes of the first drops ejected from the rim, as figure 12 shows. Finally, as a further test for our theory, we have compared in figure 16 of Appendix B, the predictions of our model with the experimental results in Thoroddsen *et al.* (2012), who studied the velocities and sizes of the fragments ejected after the impact of high speed water droplets, finding good agreement. The evidence in Appendix B indicates that the model presented here is useful not only to quantify the ejection of the fastest fragments generated after drop splashing at t_b, but also to describe the continuous drop disintegration process taking place for larger times.

5. Concluding remarks

In this contribution we present a model to predict the size and velocities of the fragments ejected after a drop impacts a smooth wall at a velocity above the critical speed described in Riboux & Gordillo (2014), also extending and providing further support to our theory in R&G. The present description can be summarized as follows: fluid particles conserve the tangential velocity given in equation (3.6), V_a^+, they possess downstream a narrow region of typical length $\sim H_a$ located where the drop meets the substrate, $\simeq \sqrt{3RVT}$. Downstream the region of length $\sim H_a$ in which the fluid is decelerated by viscous friction, the sheet is no longer in contact with the substrate and, therefore, the radial velocities of fluid particles are conserved up to the radial position where the rim is located. The rim itself is accelerated radially outwards as a consequence of the influx of momentum transported by fluid particles ejected from $\simeq \sqrt{3RVT}$ and is decelerated due to the action of the capillary forces. The rim, of initial thickness $H_t(T_e) \ll R$, also translates in the direction perpendicular to the wall thanks to the initial vertical velocity

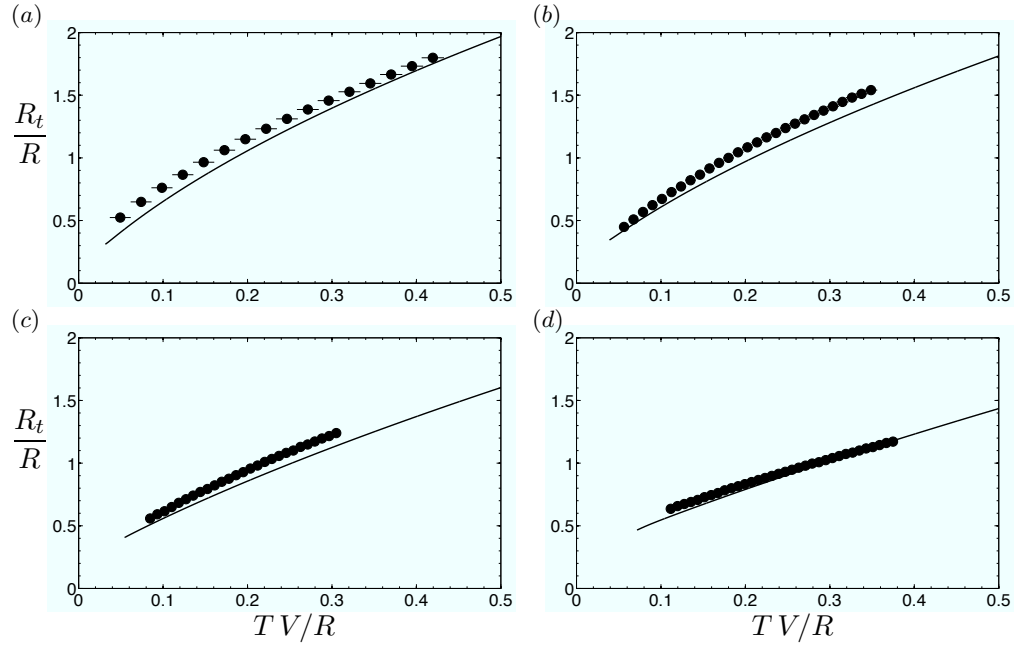

FIGURE 9. Horizontal position of the edge of the lamella as function of time. Each figure corresponds to the different fluids listed in table 1 with (*a*) Ethanol $V/V^* = 1.15$, (*b*) Decamethyltetrasiloxane $V/V^* = 1.20$, (*c*) Poly(Dimethylsiloxane) $V/V^* = 1.24$ and (*d*) 10 cP Silicone Oil $V/V^* = 1.00$. Continuous lines indicate the results of the model.

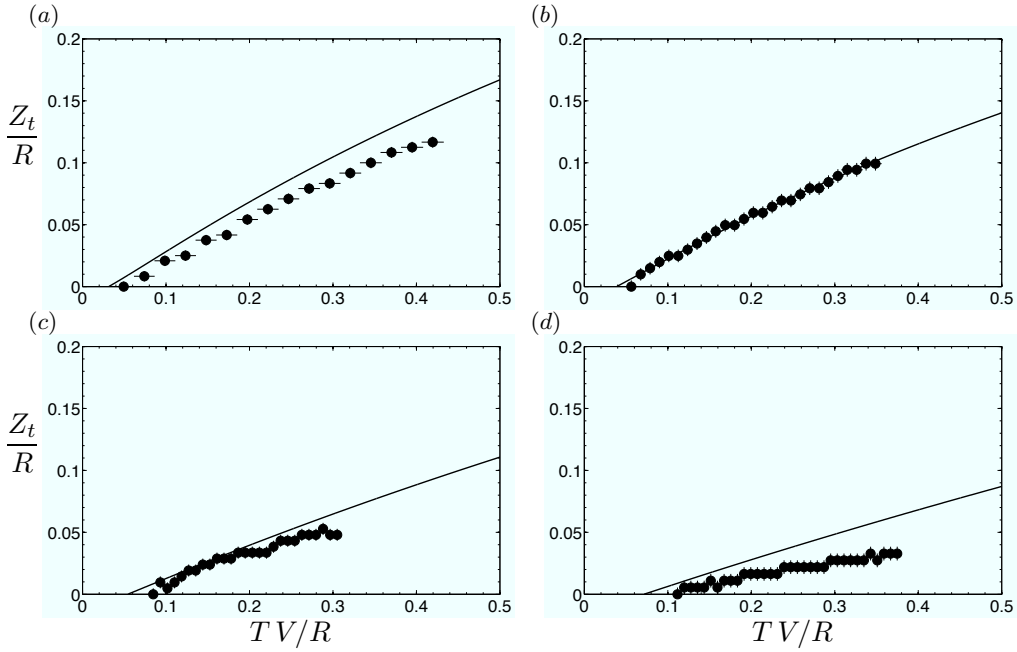

FIGURE 10. Vertical position of the edge of the lamella as function of time. Each figure corresponds to the different fluids listed in table 1 with (*a*) Ethanol $V/V^* = 1.15$, (*b*) Decamethyltetrasiloxane $V/V^* = 1.20$, (*c*) Poly(Dimethylsiloxane) $V/V^* = 1.24$ and (*d*) 10 cP Silicone Oil $V/V^* = 1.00$. Continuous lines indicate the results of the model.

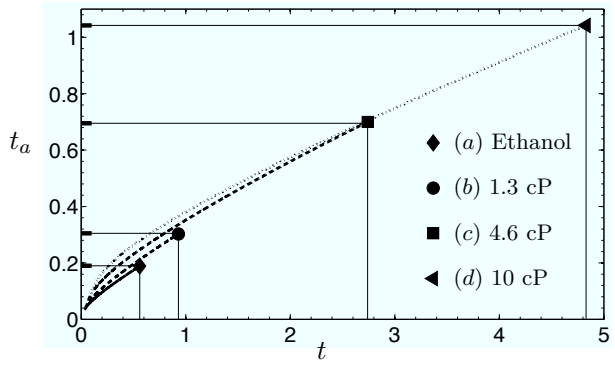

FIGURE 11. In the vertical axis, t_a indicates the instant at which the fluid particle entering the rim at instant t was ejected from the root of the lamella. The symbols indicate the breakup times $t = t_b$ for the cases: (a) Ethanol $V/V^* = 1.11$, (b) Decamethyltetrasiloxane $V/V^* = 1.21$, (c) Poly(Dimethylsiloxane) $V/V^* = 1.26$ and (d) 10 cP Silicone Oil $V/V^* = 1.12$.

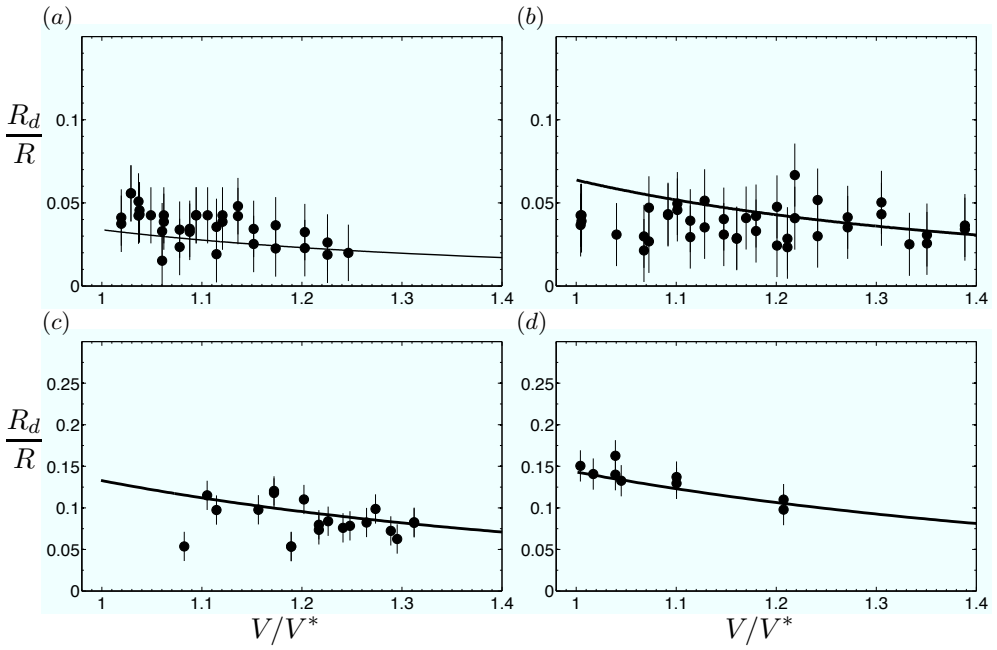

FIGURE 12. Comparison of the predicted radius of the first droplets ejected with the experiments for (a) Ethanol, (b) Decamethyltetrasiloxane, (c) Poly(Dimethylsiloxane) and (d) 10 cP Silicone Oil.

initially imparted by the lift force per unit length, ℓ, given in equation (3.2) as well as by the lift force $1/2\rho_g V_t^2 H_t C_l$; capillarity contributes to decelerate the rim vertically. Finally, droplets are ejected because the development of capillary and Rayleigh–Taylor instabilities, favor the generation of corrugations of increasing amplitude which give rise to the formation and ejection of drops at the instant when the ratio T_h/T_c is large enough. Here we have characterized this instant T_b as that for which T_c/T_h reaches a minimum, with $T_c/T_h \simeq 0.075$. Here, T_h and T_c denote the characteristic times of growth of the rim thickness and of capillary instabilities, respectively. The diameters of the drops are close

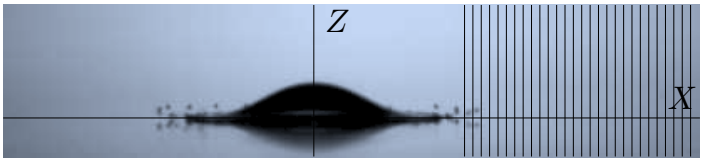

FIGURE 13. Image showing the vertical grid lines used to predict the velocity of the first ejected droplets.

to the diameter of the rim at T_b and their velocities are approximately equal to the rim velocity at this instant.

Let us point out here that these results are valid for the case of smooth and partially wetting solids with a static contact angle $\sim 20^o$. We would like to extend the theory in R&G for a wider range of static contact angles and also, for rough surfaces.

This work has been supported by the Spanish MINECO under Project DPI2011-28356-C03-01, partly financed through European funds.

Appendix A. Detection of the ejected droplets

The axisymmetry of the drop ejection process, which is recorded in a focus plane perpendicular to the solid substrate, suggests to divide each of the images composing the experimental video sequence in two symmetrical parts with respect to the line perpendicular to the point where the drop first touches the substrate, $X = 0$ (see figure 13). The image processing algorithm developed here follows in time the position of the fastest droplets ejected in each of the sides ($X \lessgtr 0$) and also provides their equivalent radii. For that purpose, the algorithm computes first the time evolution of the variance of the grey intensity at each of the vertical lines composing the Eulerian meshgrid depicted in figure 13. Due to the fact that the disintegration process does not take place in a preferential azimuthal direction, the analysis of the experimental information obtained at the focus plane is enough to describe the full drop ejection process. Figure 14(a) reveals that there exists an instant, marked with a circle, for which the variance of the grey level of each of the vertical lines experiences an abrupt change in time. Since this is precisely the instant at which the fastest drop reaches a fixed horizontal distance from the impact point, the slope of the line depicted in figure 14(b) (in pixels/s) is proportional to the horizontal velocity of the first drop ejected in the focus plane. This velocity is used to estimate the horizontal position of the first ejected drop, and this information is used to define a box that encloses the drop and moves at the predicted horizontal velocity. The position (X_d,Z_d) of the barycenter of the drop as well as its area A are obtained using the image processing toolbox of Matlab. The horizontal and vertical velocity components of the first ejected drop are then accurately calculated as $V_t = \mathrm{d}X_d/\mathrm{d}T$ and $V_v = \mathrm{d}Z_d/\mathrm{d}T$, whereas the equivalent radius is $R_d = \sqrt{A/\pi}$, as shown in figure 15.

Appendix B. Predictions of the model with the experimental results in Thoroddsen *et al.* (2012)

The limitations in the spatiotemporal resolution of our experimental setup prevented us from studying the details of the disintegration of splashing water droplets. Consequently, our experimental study does not cover a significative variation of the interfacial tension coefficient. Thus, to further validate our model, we make use in figure 16 of the experimental data in Thoroddsen *et al.* (2012), where the velocities of the fragments ejected

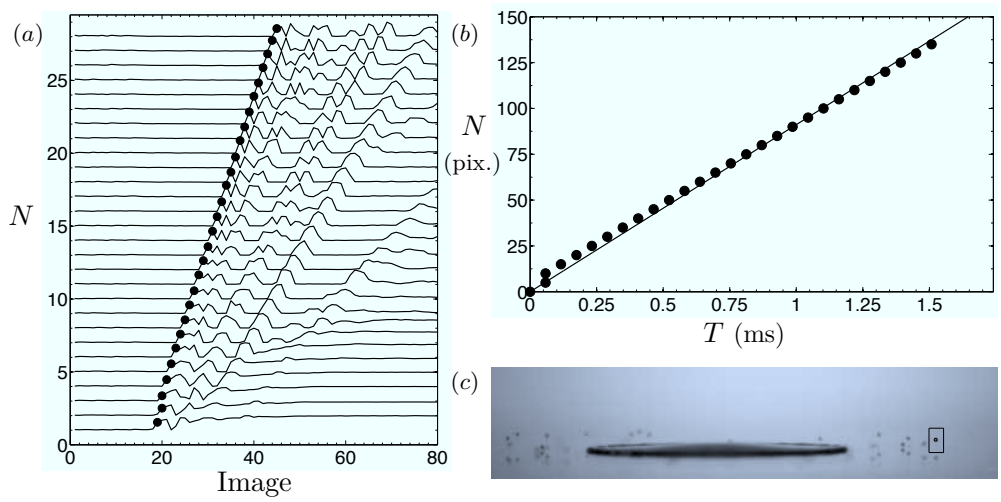

FIGURE 14. (*a*) Evolution of the variance of the grey intensity as function of the image sequence for each of the different vertical lines used in the predictor step. The black marker point indicates the instant at which the fastest droplet crosses a given vertical line. (*b*) Horizontal position of the black marker point in (*a*) as function of time. (*c*) Detection of the droplet position and the droplet area by means of box moving at the predicted horizontal velocity.

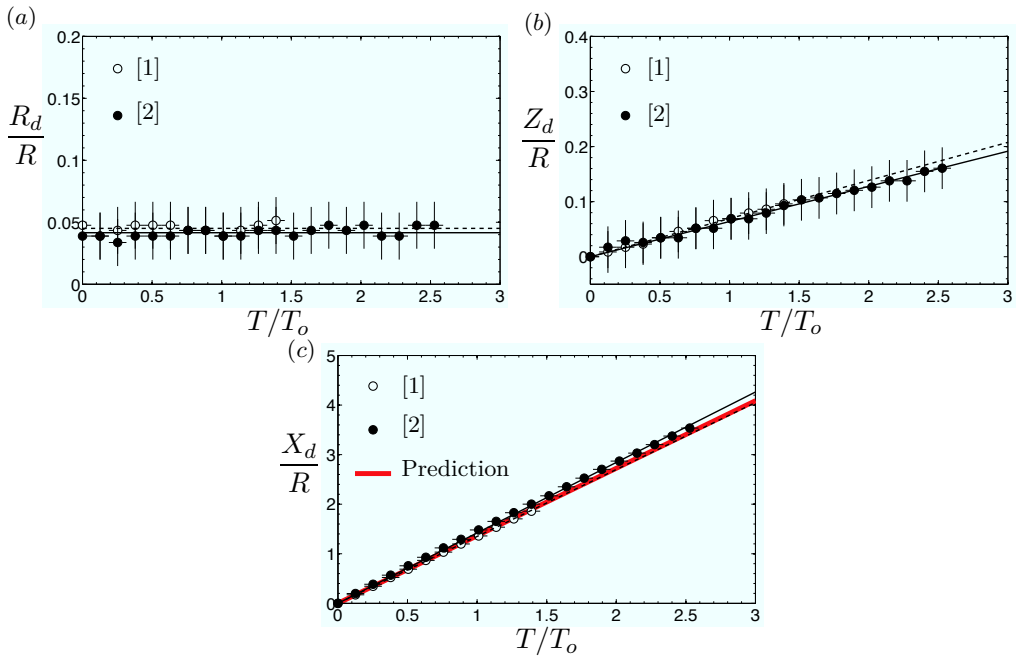

FIGURE 15. Droplet equivalent radius (*a*). Vertical (*b*) and horizontal (*c*) velocity components of the fastest droplets ejected in the regions $X > 0$ [1] and $X < 0$ [2]. The red line in figure (*c*) represents the horizontal velocity calculated in the predictor detection process, see figure 14(*b*).

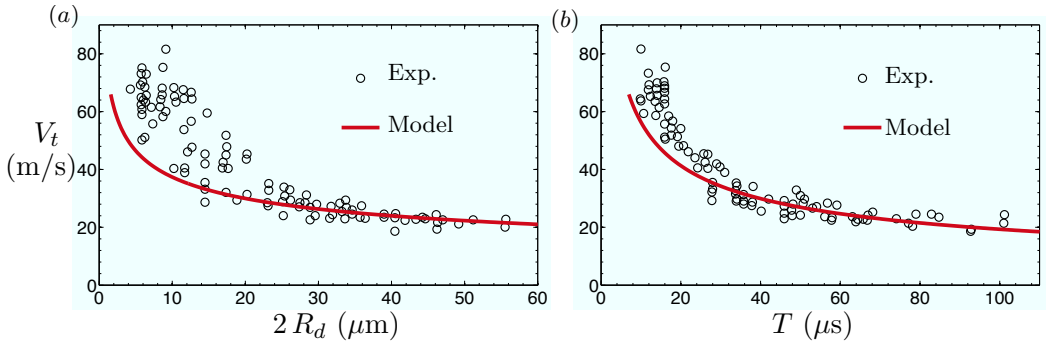

FIGURE 16. (*a*) Comparison between the experimental velocity of the droplets ejected as a function of their diameter provided in figure 5a of Thoroddsen *et al.* (2012) and the predicted velocity of the fragments, $V\,v_a^+$, plotted as a function of $R\,h_a^+ \simeq 2\,R_d$, with v_a^+ and h_a^+ given in (3.5)–(3.6). (*b*) Comparison between the velocity of the fragments ejected as a function of the time after impact given in figure 5*b* of Thoroddsen *et al.* (2012) and the predicted velocity, $V\,v_a^+$, given in equation (3.6). The fluid used by Thoroddsen *et al.* (2012) is water and the Reynolds number based on the drop radius is $Re \approx 1.45 \times 10^4$. The ejection time calculated through equation (3.1) using the experimental parameters in Thoroddsen *et al.* (2012) is $T_e \simeq 7$ μs, in agreement with the experimental observations.

after the splashing of a water droplet of diameter ~ 5.5 mm impacting onto a smooth substrate at a velocity $V \simeq 5$ m.s^{-1}, are represented as a function of both their sizes and the time after impact. The high impact speed of the drops analyzed in Thoroddsen *et al.* (2012), inhibits the formation of a long lamella; in fact, the fragments are ejected slightly downstream the root of the jet i.e., drops are ejected from $r_t \simeq a(t)$. Therefore, in order to compare with these experimental results, figure 16a represents the values of $V\,v_a^+$ as a function of $R\,h_a^+$ and in figure 16*b*, we plot $V\,v_a^+$ as a function of the time after impact, with v_a^+ and h_a^+ calculated using equations (3.5)–(3.6) for times $t \geqslant t_e$, with t_e given by equation (3.1). Figure 16 shows that our model is able to faithfully capture the ejection time as well as the velocities and sizes of the drops ejected for times slightly above t_e. Indeed, note that the fragmentation process for times closer to t_e, are affected by the phase of oscillation of the impacting droplets, which are deformed away from the spherical shape due to air resistance Thoroddsen *et al.* (2012), a fact explaining the slight deviation of the prediction for times below 15 μs. Moreover, Thoroddsen *et al.* (2012), reports the value of the ejection time for impacting droplets with values of the Reynolds and Weber numbers based on R, $Re = 9900$ and $We = 490$, $T_e \sim 10$ μs, a value that possesses an uncertainty of $\simeq 1\mu$s since the acquisition frequency is 5×10^5 frames per second. The value of the ejection time calculated using equation (3.1) is $T_e \simeq 12$ μs. All these evidences suggest that the model presented here is useful not only to quantify the ejection of the fastest fragments generated after drop splashing at t_b, but also to describe the continuous drop disintegration process taking place for larger times.

REFERENCES

AGBAGLAH, G., JOSSERAND, C. & ZALESKI, S. 2013 Longitudinal instability of a liquid rim. *Phys. Fluids* **25**, 022103.

BIRD, J. C., DHIMAN, R., KWON, H-M & VARANASI, K. K. 2013 Reducing the contact time of a bouncing drop. *Nature* **503**, 385–388.

BIRD, J. C., TSAI, S. S. H. & STONE, H. A. 2009 Inclined to splash: triggering and inhibiting a splash with tangential velocity. *New J. Phys.* **11**, 063017.

CULICK, F E C 1960 Comments on a ruptured soap film. *J. Appl. Phys.* **31**, 1128.

Driscoll, M. M., Stevens, C. S. & Nagel, S. R. 2010 Thin film formation during splashing of viscous liquids. *Phys. Rev. E* **82**, 036302.

Duchemin, L. & Josserand, C. 2011 Curvature singularity and film-skating during drop impact. *Phys. Fluids* **23**, 091701.

Duez, C., Ybert, C., Clanet, C. & Bocquet, L. 2007 Making a splash with water repellency. *Nat. Phys.* **3**, 180–183.

Eggers, J., Fontelos, M. A., Josserand, C. & Zaleski, S. 2010 Drop dynamics after impact on a solid wall: Theory and simulations. *Phys. Fluids* **22**, 062101.

Eggers, J. & Villermaux, E. 2008 Physics of liquid jets. *Rep. Prog. Phys.* **71** (3), 036601/1–79.

Gekle, S. & Gordillo, J. M. 2010 Generation and breakup of worthington jets after cavity collapse. part 1. jet formation. *J. Fluid Mech.* **663**, 293–330.

Josserand, C. & Zaleski, S. 2003 Droplet splashing on a thin liquid film. *Phys. Fluids* **15**, 1650–1657.

Kolinski, J. M., Rubinstein, S. M., Mandre, S., Brenner, M. P., Weitz, D. A. & Mahadevan, L. 2012 Skating on a film of air: Drops impacting on a surface. *Phys. Rev. Lett.* **108**, 074503.

Latka, A., Strandburg-Peshkin, A., Driscoll, M. M., Stevens, C. S. & Nagel, S. R. 2012 Creation of prompt and thin-sheet splashing by varying surface roughness or increasing air pressure. *Phys. Rev. Lett.* **109**, 054501.

Lhuissier, H. & Villermaux, E. 2011 The destabilization of an initially thick liquid sheet edge. *Phys. Fluids* **23**, 091705.

Mandre, S., Mani, M. & Brenner, M. P. 2009 Precursors to splashing of liquid droplets on a solid surface. *Phys. Rev. Lett.* **102**, 134502.

Mundo, C., Sommerfeld, M. & Tropea, C. 1995 Droplet-wall collisions: Experimental studies of the deformation and breakup process. *Int. J. Multiphase Flow* **21**, 151–173.

Palacios, J., Hernandez, J., Gomez, P., Zanzi, C. & Lopez, J. 2013 Experimental study of splashing patterns and the splashing/deposition threshold in drop impacts onto dry smooth solid surfaces. *Exp. Therm. Fluid Sci.* **44**, 571–582.

Peters, I. R., van der Meer, D. & Gordillo, J. M. 2013 Splash wave and crown breakup after disc impact on a liquid surface. *J. Fluid Mech.* **724**, 553–580.

Riboux, G. & Gordillo, J. M. 2014 Experiments of drops impacting a smooth solid surface: A model of a critical impact speed for drop splashing. *Phys. Rev. Lett.* **113**, 024507.

Richard, D., Clanet, C. & Quere, D. 2002 Contact time of a bouncing drop. *Nature* **417**, 811.

Rioboo, R., Marengo, M. & Tropea, C. 2002 Time evolution of liquid drop impact onto solid, dry surfaces. *Exp. Fluids* **33**, 112–124.

Stevens, C. S. 2014 Scaling of the splash threshold for low-viscosity fluids. *Europhys. Lett.* **106**, 24001.

Taylor, G. I. 1959 The Dynamics of Thin Sheets of Fluid. II. Waves on Fluid Sheets. *Proc. R. Soc. A* **253** (1274), 296–312.

Thoroddsen, S. T., Takehara, K. & Etoh, T. G. 2012 Micro–splashing by drop impacts. *J. Fluid Mech.* **706**, 560–570.

Villermaux, E. & Bossa, B. 2011 Drop fragmentation on impact. *J. Fluid Mech.* **668**, 412–435.

Worthington, A. M. 1908 A study of splashes. *Longman and Green, London* .

Xu, L., Zhang, W. W & Nagel, S. R. 2005 Drop splashing on a dry smooth surface. *Phys. Rev. Lett.* **94**, 184505.

Yarin, A. L. 2006 Drop impact dynamics: Splashing, spreading, receding, bouncing... *Ann. Rev. Fluid Mech.* **38**, 159–192.